X-RAY DIFFRACTION CRITERIA FOR THE IDENTIFICATION OF *TRANS*- AND *CIS*-VACANT VARIETIES OF DIOCTAHEDRAL MICAS

Bella B. Zviagina*, Boris A. Sakharov and Victor A. Drits

Geological Institute of the Russian Academy of Science, Pyzhevsky per. 7, 119017 Moscow, Russia

Abstract—To provide structural and diffraction criteria for the identification of *trans*-vacant (*tv*) and *cis*-vacant (*cv*) mica varieties with different layer stackings, powder X-ray diffraction (XRD) patterns have been simulated for $1M$, $2M_1$, $2M_2$, $3T$ and $2O$ structural models consisting of either *tv* or *cv* layers. The differences in the unit-cell parameters resulting from the specific structural distortions of *tv* and *cv* layers lead to the differences in the positions of reflections having the same indices in the XRD patterns for *tv* and *cv* $1M$, $2M_1$ and $2M_2$ mica varieties. The *tv* $1M$, $2M_1$ and $2M_2$ varieties of Al-rich micas can therefore be distinguished from the corresponding *cv* varieties using powder XRD diffraction provided that the *d* values are measured with high precision and accurately compared with those calculated from the unit-cell parameters for the corresponding *hkl* indices. The differences in reflection positions for these *tv* and *cv* varieties should decrease with increasing Mg and/or Fe contents, thus complicating their identification.

The peak positions and intensity distributions in the XRD pattern for the *tv* $3T$ variety are similar to those for the *cv* $3T$ structure with the vacancy in the right-hand *cis* site ($3T$-*cv*1), and both XRD patterns are similar to that for the $1M$-*cv* mica. The simulated XRD pattern for the *cv* $3T$ structure with the vacancy in the left-hand *cis* site ($3T$-*cv*2) is similar to that for the $1M$-*tv* variety. The similarities and dissimilarities in intensity distribution between the XRD patterns simulated for the $1M$ and $3T$ varieties in question may be associated with the differences in the mutual arrangement of cations and anions in successive layers.

Possible interstratification of *tv* and *cv* layers within the same structure should seriously complicate the identification of dioctahedral mica polytypes and polymorphs.

Key Words—*Cis*- and *Trans*-vacant Structure, Dioctahedral Mica, Polymorph, Polytype, Simulation of XRD Patterns.

INTRODUCTION

Analysis of polytypism and polymorphism of layer minerals and dioctahedral phyllosilicates in particular is an important aspect of the general problem of structural and chemical heterogeneity in minerals. A 2:1 layer consists of two tetrahedral sheets linked through an octahedral sheet. In the general case the octahedral sheet contains three symmetrically independent sites that differ in the arrangement of OH groups and oxygen anions coordinating octahedral cations: in the *trans* octahedra the OH groups lie across the space diagonal whereas in the *cis* octahedra the OH groups form a shared edge. For a long time it was commonly accepted that in dioctahedral phyllosilicates and in micas in particular, the *trans* sites are vacant. This concept was based on single-crystal structure refinements where octahedral cations in the 2:1 layers of various polytypes of muscovite, phengite, paragonite and margarite had been shown to occupy only the *cis* sites (Bailey, 1984). Dioctahedral micas therefore were treated in terms of six simple polytype structures consisting of *trans*-vacant (*tv*) centrosymmetric 2:1 layers.

The existence of 2:1 dioctahedral phyllosilicates with one of the two symmetrically independent *cis* octahedra vacant was first reported by Méring and Oberlin (1971) for a sample of Wyoming montmorillonite. Drits *et al.* (1984) were the first to deduce unit-cell parameters and atomic coordinates for a one-layer monoclinic *cis*-vacant (*cv*) illite model ($1M$-*cv*). These authors calculated powder XRD patterns for periodic $1M$-*cv* and $1M$-*tv* structures, as well as for models in which *tv* and *cv* layers were interstratified. Zvyagin *et al.* (1985) were the first to describe a monomineral Al-rich $1M$-*cv* mica sample. Monomineral $1M$-*cv* illite was also found by Drits *et al.* (1993) and Lee (1996). Reynolds and Thomson (1993), Drits *et al.* (1993) and Lanson *et al.* (1996) described an association of periodic $1M$-*cv* and $1M$-*tv* illite polymorphs. Zhukhlistov *et al.* (1996) studied monomineral $1M$-*cv* sericite and associations of $1M$-*cv* and $1M$-*tv* sericites. Reynolds (1993), McCarty and Reynolds (1995) and Drits *et al.* (1996) showed that the *cv* structure exists in illite fundamental particles of illite-smectites (I-S) exhibiting the $1M$ and $1M_d$ stacking sequences, and that *cv* 2:1 layers are commonly interstratified with *tv* layers in these illite stackings. The coexistence of *cv* and *tv* layers in I-S formed in volcanic and sedimentary rocks has been described in many papers (McCarty and Reynolds, 1995, 2001; Altaner and Ylagan, 1997; Cuadros and Altaner, 1998a, 1998b; Ylagan *et al.*, 2000; Lindgreen *et al.*, 2000; Drits *et al.*, 2002).

* E-mail address of corresponding author:
zviagina@ginras.ru

467

It seems logical therefore that other polytypes of dioctahedral micas having *cv* structure may also exist and the whole diversity of mica structures may appear much more complicated than was previously imagined. This was taken into account in the nomenclature of dioctahedral micas developed by Zvyagin (2001). The possible dioctahedral mica structures are classified into two groups according to the 2:1 layer structure, either *tv* or *cv*. The *tv* group contains the six classical polytypes, whereas the *cv* family is in its turn subdivided into two subgroups depending on the distribution of the octahedral cations over the available *cis* sites. In the first subgroup, the octahedral vacancy is in one of the two symmetrically independent *cis* sites, either right-hand or left-hand in all the layers (*cv*1 and *cv*2 layers, respectively); in the second subgroup, *cv*1 and *cv*2 layers alternate regularly within the structure (Table 1).

Importantly, micas having the same chemical composition but differing in layer structure should be regarded as polymorphs rather than polytypes, if 2:1 layers are chosen as structural units. In other words the structures within the *tv* family or those within the *cv* family are polytypes, while structures from different families are polymorphs with respect to each other. This approach is justified by the different physical properties of micas having the same composition and distinct layer structures. In particular, *tv* and *cv* 2:1 phyllosilicates have different dehydroxylation temperatures (Drits *et al.*, 1998). Another notion introduced in the classification of Zvyagin (2001) is that of pseudopolytypes, *i.e.* micas having the same layer structure but differing in the structure of the interlayer. For example, the 1*M-tv* structure having octahedral coordination of the interlayer cation and 2*M*$_2$-*tv* with the interlayer cation in a hexagonal prism are pseudopolytypes, whereas the 1*M-tv*, 2*M*$_1$-*tv* and 3*T-tv* structures are true, or simple polytypes, and so are the *tv* 2*M*$_2$ and 2*O* micas. On the whole, in terms of this approach, 18 dioctahedral mica modifications were derived falling into three groups containing six polytypes each (Table 1).

The next step should consist of developing methodologies for the identification of natural mica varieties containing *tv* and *cv* 2:1 layers and in particular, in formulating specific structural and diffraction criteria to distinguish between various *tv* and *cv* structures. Previously, this was done for a few particular cases. Diffraction criteria were determined for the identification of 1*M-tv* and 1*M-cv* micas using powder XRD (Drits *et al.*, 1993; Reynolds and Thomson, 1993) and oblique-texture electron diffraction (Zhukhlistov *et al.*, 1996). Drits *et al.* (1993) also noted that 3*T-tv* and 1*M-cv* mica polymorphs produce similar diffraction effects, *i.e.* in their XRD patterns, *hkl* reflections have similar intensities and close positions. These authors showed that all illite varieties previously described as 3*T-tv* (Warshaw, 1959; Ey, 1984; Halter, 1988) in fact correspond to 1*M-cv* (Drits *et al.*, 1993). Zhukhlistov *et al.* (1996) formulated criteria to distinguish between 1*M-tv* and 1*M-cv* sericites, as well as between a mixture of the 1*M-tv* and 1*M-cv* and that of 1*M-tv* and 3*T-tv* sericites using oblique-texture electron diffraction. Drits and Sakharov (2004) calculated XRD patterns for dioctahedral structural models, in which *tv* and *cv* layers were interstratified and arranged as in periodic 2*M*$_1$ and 3*T* mica polytypes. They showed that the XRD patterns of interstratified *cv/tv* 2*M*$_1$ and *cv/tv* 3*T* models are similar to those of 2*M*$_1$-*tv* and 3*T-tv* mica structures, respectively, especially if the number of *cv* layers is either small or large.

The purpose of the present work has been to provide structural and diffraction criteria for the identification of *tv* and *cv* mica varieties with different layer stackings. To do this, powder XRD patterns were simulated for 1*M*, 2*M*$_1$, 2*M*$_2$, 3*T* and 2*O* structural models consisting of either *tv* or *cv* layers.

METHOD

Simulation of XRD patterns

The mathematical formalism used to calculate powder XRD patterns was described by Plançon and

Table 1. Space groups and symbols for possible dioctahedral mica polytypes and polymorphs (modified from Zvyagin, 2001).

No.	Symbol *tv, cv**	Space group *tv*	*cv**	Symbol *cv*12**	Space group *cv*12**
1	1*M*	C2/m	C2	2*M*$_1$	C2/c
2	2*M*$_1$	C2/c	C2	2*M*$_1$	Cc
3a	3*T*	P3$_1$12	P3$_1$12	6*T*	P3$_2$12
3b	3*T*	P3$_2$12	P3$_2$12	6*T*	P3$_1$12
4	2*M*$_2$	C2/c	C2	2*M*$_2$	Cc
5	2*O*	Ccmm	C222$_1$	2*O*	Cc2m
6a	6*H*	P6$_1$22	P6$_1$22	6*T*	P3$_1$12
6b	6*H*	P6$_5$22	P6$_5$22	6*T*	P3$_2$12

* vacancy either in right-hand or left-hand *cis* site
** regular alternation of layers having vacancy in right-hand and left-hand *cis* site (*cv*1 and *cv*2 layers)

Table 2. Simulated Cartesian atomic coordinates for the 1M mica structure consisting of: (a) tv layers; (b) cv1 layers; and (c) cv2 layers (a = 5.193 Å, b= 9.005 Å, c^* = 9.980 Å).

Atom	(a) x	y	z	Atom	(b) x	y	z	Atom	(c) x	y	z
M	1	0.6667	0	M1	0	0	0	M1	0	0	0
T	0.3146	0.3288	0.2702	M2	0	0.3333	0	M2	0	0.6667	0
O1	0.3091	0.3120	0.1078	T1	0.3359	0.3450	0.2702	T1	0.3359	0.6550	0.2702
O2	0.3659	0.5	0.3167	T2	0.8495	0.1738	0.2702	T2	0.8495	0.8262	0.2702
O3	0.0407	0.7262	0.3356	O1	0.3134	0.3561	0.1078	O1	0.3134	0.6439	0.1078
OH	0.3773	0	0.1028	O2	0.8774	0.1681	0.1078	O2	0.8774	0.8319	0.1078
K	0.3085	0	0.5	O3	0.0690	0.2832	0.3356	O3	0.0690	0.7168	0.3356
				O4	0.5670	0.2337	0.3167	O4	0.5670	0.7663	0.3167
				O5	0.3904	0.5094	0.3356	O5	0.3904	0.4906	0.3356
				OH	0.8113	0.4780	0.1028	OH	0.8113	0.5220	0.1028
				K	0.8457	0.5124	0.5	K	0.8457	0.4876	0.5

Tchoubar (1977), Plançon (1981), Sakharov *et al.* (1982) and, in greater detail, by Drits and Tchoubar (1990). One of the principal advantages of this approach is that it can predict diffraction effects from diverse, theoretically possible and crystal-chemically justified layer structural models. Its application makes it possible to analyze diffraction effects of various parameters describing specific features of periodic and defective structural models. For each particular model, the following structural and probability parameters should be defined: the structure and chemical composition of the coexisting layers; the azimuthal orientations, translations, reflection operations and modes of alternation of the layers; the probability parameters that describe the model quantitatively; mean size and size distribution of coherent scattering domains (CSDs) (Drits and Tchoubar, 1990).

The XRD patterns were calculated for CuKα radiation and random distribution of CSD orientations. The CSDs were disk-shaped, with the mean diameter of 500 Å. The CSDs' thicknesses were distributed lognormally along c^* (Drits *et al.*, 1997), with the mean and maximum number of layers in CSDs being 15 and 50 layers, respectively.

The indexing of reflections in the simulated XRD patterns was based on the comparison between the simulated d values with those calculated from the unit-cell parameters of the corresponding structure (see below). This has allowed us to provide more accurate indices for some of the reflections in the powder XRD patterns for dioctahedral tv 1M, 2M_1, 2M_2 and 3T micas than those previously published (*e.g.* by Bailey, 1984). It should be noted, however, that the actual numerical d values of the hkl reflections given in Tables 4−8 are valid for the specific unit-cell parameters of the corresponding structural models (Table 3).

Structural models

The orthogonal unit-cells of the tv and cv layers have the same dimensions a = 5.199 Å, b = 9.005 Å and $c \times \sin \beta$ = 9.980 Å, and composition K$_{0.80}$Na$_{0.04}$

(Al$_{1.66}$Fe$^{3+}_{0.06}$Fe$^{2+}_{0.02}$Mg$_{0.28}$)(Si$_{3.41}$Al$_{0.59}$)O$_{10}$(OH)$_2$, which correspond to a natural illite sample (Plançon *et al.*, 1985). In a projection on the *ab* plane, the displacement of the center of the ditrigonal ring of the lower tetrahedral sheet of the upper layer with respect to that of the preceding layer along the *a* axis is T$_{tv}$= −0.383a and T$_{cv}$= −0.3085a for the *tv* and *cv* 1M structures, respectively (Drits *et al.*, 1984, 2006). The atomic coordinates for these structures were obtained from the above cell parameters and cation composition using the procedure described by Drits *et al.* (2006). First, the atomic coordinates for the *tv* structure were calculated using the algorithm of Smoliar-Zviagina (1993), which is based on regression equations relating structural features and chemical composition of micaceous minerals that were obtained from the analysis of refined structural data on micas of various compositions published in the literature. Second, to obtain a *cv* structure, the upper half of the *tv* layer including the octahedral cation sites was rotated by +120º or −120º around *c** passing through the center of the vacant octahedron (to position the vacancy in the right-hand or left-hand *cis* site, respectively). The coordinates of the lower half-layer were obtained with the help of a rotation by 180º around the *b* axis in the new unit-cell. The resulting Cartesian atomic coordinates for the unit-cells of the *tv* 1M structure and 1M structure consisting of *cv*1 layers (vacancy in the right-hand *cis* site with the coordinates 0, 0.6667, 0) and *cv*2 layers (vacancy in the left-hand *cis* site with the coordinates 0, 0.3333, 0) are given in Table 2.

The structural models listed in Table 3 were constructed using *tv*, *cv*1 and *cv*2 layers with relevant layer orientations and T$_{tv}$ and T$_{cv}$ displacements between successive layers for *tv* and *cv* structures, respectively. In the structures with the 1M layer sequence, each layer has the same orientation as the preceding one. The 2M_1 polymorphs consist of regularly alternating layers rotated through ±120º with respect to each other. In the 2M_2 structures, successive layers are rotated through

Table 3. Structural models used for simulation of XRD patterns*.

Layer sequence	Structural model	Space group	a (Å)	b (Å)	c (Å)	β (º)
1M	1M-tv	C2/m	5.199	9.005	10.177	101.284
	1M-cv	C2	5.199	9.005	10.108	99.130
2M	2Mcv12	C2/c	5.199	9.005	20.059	84.303
2M$_1$	2M$_1$-tv	C2/c	5.199	9.005	20.059	95.697
	2M$_1$-cv1	C2	5.199	9.005	20.024	94.594
	2M$_1$-cv12	Cc	5.199	9.005	20.024	94.594
	2M$_1$-cv1/cv2	C2/c	5.199	9.005	20.024	94.594
3T	3T-tv	P3$_1$12	5.199		29.94	
	3T-cv1	P3$_1$12	5.199		29.94	
	3T-cv2	P3$_1$12	5.199		29.94	
	3T-cv1/cv2	P3$_1$12	5.199		29.94	
2M$_2$	2M$_2$-tv	C2/c	9.005	5.199	20.256	99.803
	2M$_2$-cv1	C2	9.005	5.199	20.152	97.924
	2M$_2$-cv12	Cc	9.005	5.199	20.152	97.924
2O	2O-tv	Ccmm	5.199	9.005	19.96	
	2O-cv1	C222$_1$	5.199	9.005	19.96	
	2O-cv12	Cc2m	5.199	9.005	19.96	

* *cv*1 refers to layers with the right-hand *cis* site vacant; *cv*2 refers to layers with the left-hand *cis* site vacant; *cv*12 refers to regular alternation of *cv*1 and *cv*2 layers; *cv*1/*cv*2 refers to *cv*1 and *cv*2 layers that occur with equal probability for each given layer orientation.

±60º. In the 3*T* structural models each layer is rotated counter-clockwise, with respect to the preceding one, by 120º, in accordance with the space group P3$_1$12. The layers in the 2*O* structures are rotated by 180º with respect to each other. The ±120º and ±60º rotations are used to generate the 2*M*$_1$ and 2*M*$_2$ polytypes instead of the symmetry elements (screw axes and glide planes) of the corresponding space groups for simplicity. This can be done as in the structures in question $b = a \sqrt{3}$. The c and β parameters for the 2*M*$_1$ and 2*M*$_2$ structural models were obtained based on the layer thickness of 9.980 Å and the following relationships:

$$c \times \cos \beta / a \ (2M_1) = c \times \cos \beta / a \ (1M);$$
$$c \times \cos \beta / a \ (2M_2) = c \times \cos \beta / a \ (1M),$$

where $a \ (2M_2) = b \ (1M)$ and $c \times \cos \beta / a \ (1M)$ is either T$_{tv}$ or T$_{cv}$.

The *tv* structures are labeled 1*M-tv*, 2*M*$_1$*-tv* etc. Structures 2*M*$_1$*-cv*1, 2*M*$_2$*-cv*1, 3*T-cv*1 and 2*O-cv*1 have the octahedral vacancy in the right-hand *cis* position; in the 3*T-cv*2 structure the octahedral vacancy is in the left-hand *cis* site. In the 2*M*$_1$*-cv*1/*cv*2 and 3*T-cv*1/*cv*2 structures layers having either right- or left-hand *cis* sites vacant occur with equal probability for each given layer orientation. In the 2*M*$_1$*-cv*12, 2*M*$_2$*-cv*12 and 2*O-cv*12 structures *cv*1 and *cv*2 layers alternate regularly. In the 2*M-cv*12 structural model *cv*1 and *cv*2 layers alternate regularly and are packed as in the 1*M* structure, *i.e.* with the same orientation for both layer types. The c and β parameters for this structure are explained in the Discussion below.

RESULTS

1M varieties

The calculated XRD patterns for the 1*M-tv* and 1*M-cv* structural models are shown in Figure 1a,b. The *hkl* indices, d_{hkl} values and relative peak intensities of the reflections are given in Table 4. The basic difference between the two XRD patterns is the presence of four reflections of similar intensity: 111, 11$\bar{2}$, 112 and 11$\bar{3}$ at 3.879 Å, 3.580 Å, 3.119 Å and 2.862 Å, respectively, in the XRD pattern for the 1*M-cv* structure, as compared with two strong reflections, 11$\bar{2}$ and 112 located at d = 3.638 Å and 3.067 Å, respectively, in the pattern for the 1*M-tv* structure. For the 1*M-tv* structure, the 11$\bar{3}$ peak is much weaker than for the 1*M-cv* variety and the 111 peak is extremely weak. The strongest peak for the 1*M-tv* structure is 020 (d = 4.502 Å) whereas the strongest reflection for the 1*M-cv* structure is 110 at 4.460 Å. In addition, the profiles of the two patterns in the region of 13*l*, 04*l* and 22*l* reflections differ substantially (Figure 1). Table 4 shows that the positions of reflections having the same indices do not coincide in the two patterns. The structural features that are responsible for these differences will be discussed below.

2M-cv12 structural model. Figure 1c shows the XRD pattern simulated for a structure termed 2*M-cv*12, in which *cv*1 and *cv*2 layers alternate regularly and are packed as in the 1*M* structure. The pattern is nearly identical to that for the 1*M-cv* structure as regards both the peak positions and intensities (Table 5) except for the region corresponding to d > 4 Å and the presence of
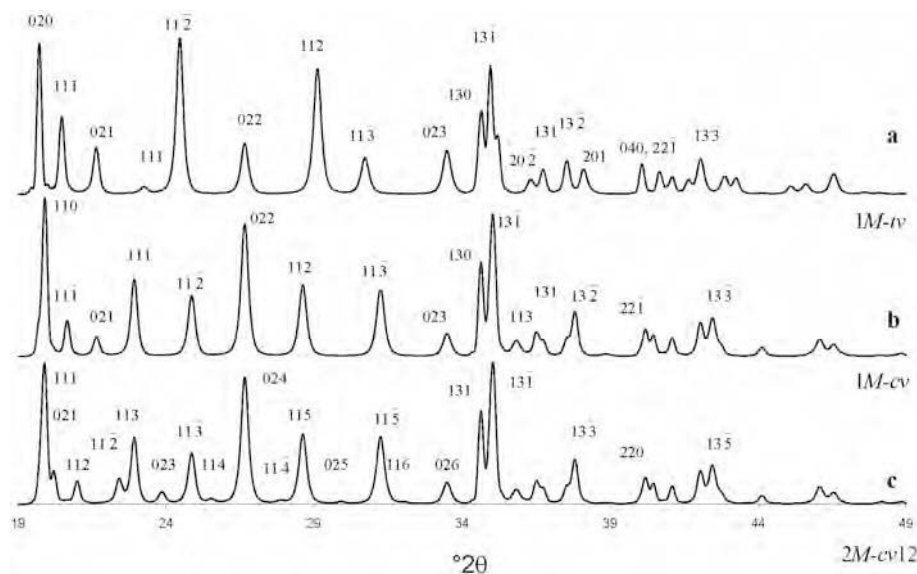
Figure 1. Simulated powder XRD patterns for structural models: (a) 1*M-tv;* (b) 1*M-cv*; and (c) 2*M-cv*12 (basal reflections are not shown). CuKα radiation.

weak maxima located at 4.396 (021), 3.965 (11$\bar{2}$), 3.729 (023), 3.489 (114), 3.201 (11$\bar{4}$), 2.987 (025) and 2.793 Å (116). The origin of these reflections will be treated in greater detail in the Discussion below.

2M_1 varieties

Figure 2 shows the XRD patterns simulated for structural models 2M_1-tv, 2M_1-cv1 and 2M_1-cv12. The

Table 4. Reflection indices, d_{hkl} values and relative peak intensities in the simulated XRD patterns for structural models 1*M-tv* and 1*M-cv*.

	1*M-tv*			1*M-cv*	
hkl	d_{hkl} (Å)	I (%)	hkl	d_{hkl} (Å)	I (%)
020	4.502	97	110	4.460	100
11$\bar{1}$	4.337	50	11$\bar{1}$	4.299	21
021	4.106	29	021	4.104	11
111	3.823	4	111	3.879	49
11$\bar{2}$	3.638	100	11$\bar{2}$	3.580	39
022	3.344	32	022	3.343	82
112	3.067	80	112	3.119	43
11$\bar{3}$	2.910	21	11$\bar{3}$	2.862	41
023	2.676	26	023	2.675	12
130	2.588	51	130	2.589	56
13$\bar{1}$	2.567	81	13$\bar{1}$	2.561	88
220	2.550	36	113	2.506	9
20$\bar{2}$	2.474	9	131	2.460	13
131	2.446	13	13$\bar{2}$	2.379	27
13$\bar{2}$	2.396	21	11$\bar{4}$	2.317	1
201	2.361	13	22$\bar{1}$	2.243	14
040, 22$\bar{1}$	2.250	18	220	2.229	12
220	2.218	12	041	2.196	10
041	2.196	10	202, 22$\bar{2}$	2.148	20
22$\bar{2}$	2.168	8	13$\bar{3}$	2.129	22
13$\bar{3}$	2.148	21			
202	2.109	10			

hkl indices, d_{hkl} values and relative peak intensities for these structures, as well as for 2M_1-*cv*1/*cv*2 are given in Table 5. The most significant differences concern the positions and intensities of the 11*l* reflections. Specifically, for the 2M_1-*tv* structure the 11$\bar{3}$ (*d* = 3.878 Å) and 115 (*d* = 2.862 Å) reflections are quite intense while the 113 (*d* = 3.579 Å) and 11$\bar{5}$ (*d* = 3.119 Å) peaks are very weak; on the contrary, for the 2M_1-*cv*1 structure the 113 (*d* = 3.609 Å) and 11$\bar{5}$ (*d* = 3.093 Å) reflections are fairly strong whereas 11$\bar{3}$ (*d* = 3.849 Å) and 115 (*d* = 2.886 Å) are weak. Interestingly, the strongest reflection for the 2M_1-*tv* structure is 11$\bar{1}$ (*d* = 4.465 Å) whereas the strongest peak for the 2M_1-*cv*1 structure is 020,110 at 4.495 Å.

The characteristic feature of the XRD pattern for 2M_1-*cv*12, a structure where *cv*1 and *cv*2 layers alternate regularly (Figure 2c, Table 5), is the presence of the 11$\bar{2}$ reflection located at 4.207 Å, which is absent in the other 2M_1 structures. Otherwise this pattern is similar to that for the 2M_1-*cv*1 structure except for the following minor differences: (a) unlike 2M_1-*cv*1, the XRD pattern for the 2M_1-*cv*12 structure does not contain the 11$\bar{3}$ reflection; (b) the 021 reflection (*d* = 4.390 Å) is quite strong in the 2M_1-*cv*12 structure, whereas in the 2M_1-*cv*1 structure, it is weak.

The pattern calculated for a structure where *cv*1 and *cv*2 layers occur with equal probability for each given layer orientation, 2M_1-*cv*1/*cv*2 (figure not shown), is very similar to that for the 2M_1-*cv*12 structure except for the intensity distribution in the region 3.996 Å ⩽ *d* ⩽ 4.390 Å. (Table 5).

2M_2 varieties

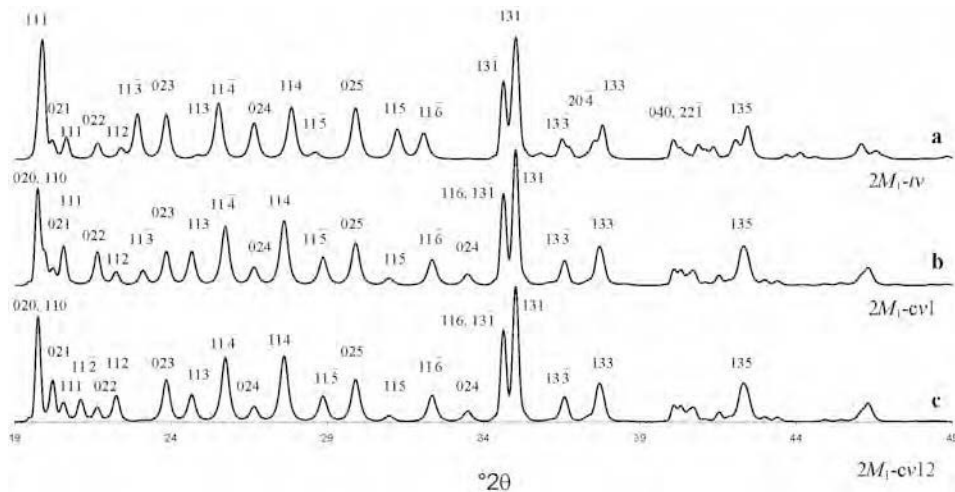Figure 3 shows the XRD patterns simulated for the 2M_2-*tv,* 2M_2-*cv*1 and 2M_2-*cv*12 structures. The *hkl*

Figure 2. Simulated powder XRD patterns for structural models: (a) $2M_1$-tv; (b) $2M_1$-cv1; and (c) $2M_1$-cv12 (basal reflections are not shown). CuKα radiation.

indices, d_{hkl} values and relative peak intensities are given in Table 6. The XRD pattern for the $2M_2$-tv structure differs from those for the cv structures, in the number of peaks, their positions and intensities. Specifically, for the $2M_2$-tv variety the $20\bar{4}$, $11\bar{4}$, 114 and 204 reflections at 3.638 Å, 3.489 Å, 3.202 Å and 3.067 Å, respectively, have similar intensities, while for both cv structures, $11\bar{4}$ ($d = 3.461$ Å) and 114 ($d =$

3.229 Å) are stronger than $20\bar{4}$ ($d = 3.581$ Å) and 204 ($d = 3.115$ Å). An important diagnostic feature is that the $2M_2$-tv variety shows the $11\bar{3}$ ($d = 3.878$ Å) and 115 ($d = 2.863$ Å) reflections, which are absent in the XRD patterns for the cv structures. Instead, the XRD patterns for the $2M_2$-cv1 and $2M_2$-cv12 structures contain reflections 113 ($d = 3.604$ Å) and $11\bar{5}$ ($d = 3.100$ Å) which partly overlap with $20\bar{4}$ and 204, respectively

Table 5. Reflection indices, d_{hkl} values and relative peak intensities in the simulated XRD patterns for structural models $2M_1$-tv, $2M_1$-cv1, $2M_1$-cv12 , $2M_1$-cv1/cv2 and $2M$-cv12.

| | $2M_1$-tv | | | $2M_1$-cv | | $2M_1$-cv1 | $2M_1$-cv12 | $2M_1$-cv1/cv2 | | $2M$-cv12 | |
hkl	d_{hkl} (Å)	I (%)	hkl	d_{hkl} (Å)	I (%)	I (%)	I (%)	hkl	d_{hkl} (Å)	I (%)
$11\bar{1}$	4.465	98	020, 110	4.495	72	78	74	111	4.463	100
021	4.396	16	021	4.390	13	30	18	021	4.396	23
111	4.300	18	111	4.318	29	13	19	112	4.230	16
022	4.104	12	$11\bar{2}$	4.207	–	15	–	$11\bar{2}$	3.965	18
112	3.967	8	022	4.105	23	10	12	113	3.879	47
$11\bar{3}$	3.878	38	112	3.996	9	19	11	023	3.729	8
023	3.730	38	$11\bar{3}$	3.849	10	–	–	$11\bar{3}$	3.580	35
113	3.579	2	023	3.730	23	30	25	114	3.489	3
$11\bar{4}$	3.489	46	113	3.609	23	20	20	024	3.343	89
024	3.343	30	$11\bar{4}$	3.461	42	48	41	$11\bar{4}$	3.201	2
114	3.202	42	024	3.343	13	11	11	115	3.119	48
$11\bar{5}$	3.119	4	114	3.229	49	49	46	025	2.987	1
025	2.987	41	$11\bar{5}$	3.093	20	19	19	$11\bar{5}$	2.862	47
115	2.862	21	025	2.987	30	31	30	116	2.793	1
$11\bar{6}$	2.789	20	115	2.886	4	4	3	026	2.675	15
$13\bar{1}$	2.589	62	$11\bar{6}$	2.767	20	20	19	131	2.589	65
131	2.561	100	026	2.676	9	8	8	$13\bar{1}$	2.561	100
$11\bar{7}$	2.506	3	116, $13\bar{1}$	2.589	63	68	67	117	2.506	10
$13\bar{3}$	2.460	16	131	2.561	97	98	99	133	2.460	14
$20\bar{4}$	2.394	12	$13\bar{3}$	2.455	19	19	18	$13\bar{3}$	2.379	30
133	2.379	26	133	2.385	29	29	27	$11\bar{7}$	2.317	1
040, $22\bar{1}$	2.250	16	040, $22\bar{1}$	2.249	10	10	11	220	2.243	19
221	2.208	12	041	2.237	10	10	11	222,135	2.229	15
$22\bar{3}$	2.183	10	$13\bar{5}$, 221	2.216	9	9	10	042	2.196	11
222	2.148	13	$22\bar{3}$	2.174	7	7	7	$22\bar{2}$,206	2.148	21
135	2.129	25	135	2.136	30	30	27	$13\bar{5}$	2.129	26
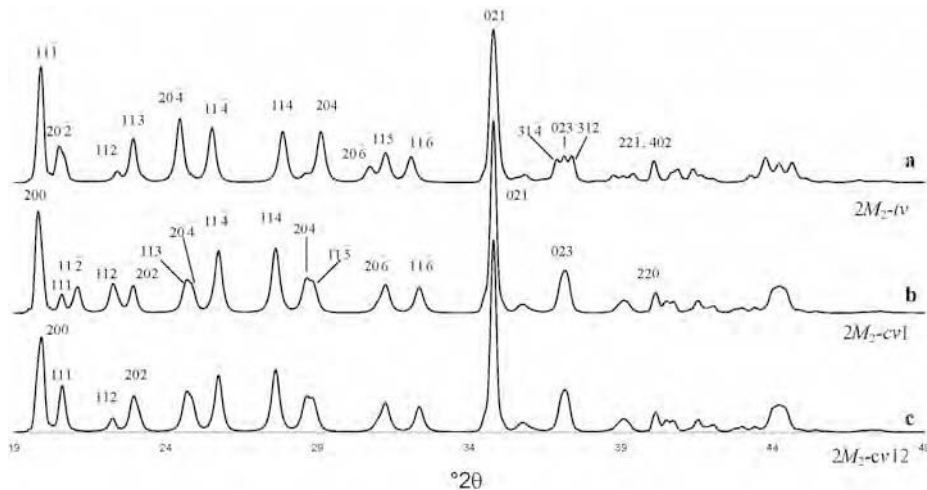
Figure 3. Simulated powder XRD patterns for structural models: (a) $2M_2$-tv; (b) $2M_2$-cv1; and (c) $2M_2$-cv12 (basal reflections are not shown). CuKα radiation.

(Figure 3, Table 6). This overlap is due to the $20\bar{4}$ and $11\bar{4}$ reflections of the cv varieties having smaller d values, and 114 and 204, greater d values, as compared to the positions of these reflections in the XRD pattern of the $2M_2$-tv structure.

Another distinguishing feature of the $2M_2$-tv variety is the presence of three closely spaced reflections, $31\bar{4}$ at $d = 2.436$ Å, 023 at $d = 2.421$ Å and 312 at $d = 2.406$ Å, whereas both cv varieties show a single 023 reflection at $d = 2.419$ Å.

The patterns for the $2M_2$-cv1 and $2M_2$-cv12 structures are nearly identical but for the following differences.

First, the pattern for the $2M_2$-cv1 structure contains reflections $11\bar{2}$ ($d = 4.212$ Å) and 112 ($d = 3.992$ Å), the former being absent and the latter, very weak, in both the XRD patterns for the $2M_2$-tv and $2M_2$-cv12 structures. Second, the 111 peak at 4.317 Å in the pattern for the $2M_2$-cv12 structure is much stronger than it is for the $2M_2$-cv1 structure. (Figure 3, Table 6).

3T varieties

The XRD patterns simulated for structures $3T$-tv, $3T$-cv1 and $3T$-cv2 are shown in Figure 4. The corresponding reflection indices, positions and intensities for

Table 6. Reflection indices, d_{hkl} values and relative peak intensities in the simulated XRD patterns for structural models $2M_2$-tv, $2M_2$-cv1 and $2M_2$-cv12.

|	tv		$cv1$, $cv12$		$cv1$	$cv12$
hkl	d_{hkl} (Å)	I (%)	hkl	d_{hkl} (Å)	I (%)	I (%)
$11\bar{1}$	4.464	75	200	4.461	51	50
$20\bar{2}$	4.333	22	111	4.317	9	23
112	3.967	7	$11\bar{2}$	4.212	12	–
$11\bar{3}$	3.878	29	112	3.992	13	8
$20\bar{4}$	3.638	41	202	3.879	12	19
$11\bar{4}$	3.489	34	113	3.604	17	21
114	3.202	31	$20\bar{4}$	3.581	16	20
204	3.067	31	$11\bar{4}$	3.461	30	29
$20\bar{6}$	2.909	10	114	3.229	31	31
115	2.863	19	204	3.115	19	19
$11\bar{6}$	2.789	14	$11\bar{5}$	3.100	18	18
021	2.578	99	$20\bar{6}$	2.863	15	15
311	2.506	3	$11\bar{6}$	2.767	12	12
$31\bar{4}$	2.436	13	021	2.578	100	100
023	2.421	17	$31\bar{3}$	2.510	3	5
312	2.406	17	023	2.419	21	21
$31\bar{5}$	2.323	5	024	2.304	8	8
024	2.305	4	220	2.246	10	10
$31\bar{3}$	2.287	6	$22\bar{2}$	2.227	7	7
$22\bar{1}$, $40\bar{2}$	2.249	12	221	2.216	7	7
221	2.208	8	$22\bar{3}$	2.174	8	8
$22\bar{3}$, 025	2.182	8	$40\bar{4}$	2.150	3	3
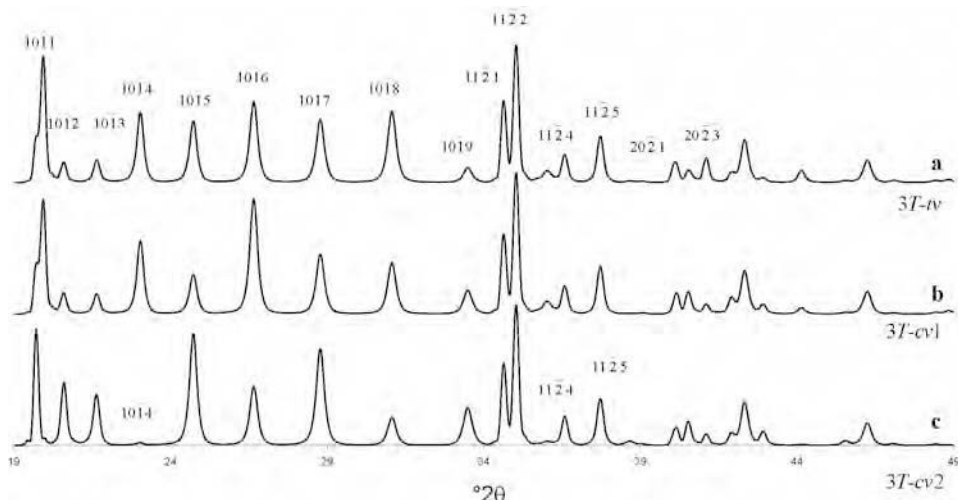
Figure 4. Simulated powder XRD patterns for structural models: (a) 3*T-tv*; (b) 3*T-cv*1; and (c) 3*T-cv*2 (basal reflections are not shown). CuKα radiation.

these varieties, as well as for the 3*T-cv*1/*cv*2 structure are given in Table 7. In the XRD patterns for the 3*T-tv*, 3*T-cv*1 and 3*T-cv*2 structures, the peak positions are identical. For the first two varieties the intensity distributions are similar except for a few minor differences. For the 3*T-tv* structure, the 10$\bar{1}$5 reflection (d = 3.600 Å) is only slightly weaker than the 10$\bar{1}$4 (d = 3.859 Å) peak while the 3*T-cv*1 variety, shows greater differences in the intensities of these reflections. Moreover, the four reflections 10$\bar{1}$4, 10$\bar{1}$5, 10$\bar{1}$7 and

Table 7. Reflection indices, d_{hkl} values and relative peak intensities in the simulated XRD patterns for structural models 3*T-tv*, 3*T-cv*1, 3*T-cv*2 and 3*T-cv*1/*cv*2.

hkl	d_{hkl} (Å)	I (%)			
		tv	cv1	cv2	cv1/cv2
10$\bar{1}$0	4.500	32	36	82	62
10$\bar{1}$1	4.452	92	81	–	33
10$\bar{1}$2	4.313	14	14	45	20
10$\bar{1}$3	4.104	15	13	37	16
10$\bar{1}$4	3.859	50	51	1	19
10$\bar{1}$5	3.600	43	28	80	50
10$\bar{1}$6	3.343	58	90	41	60
10$\bar{1}$7	3.101	45	41	68	52
10$\bar{1}$8	2.878	50	33	19	26
10$\bar{1}$9	2.676	10	13	26	19
11$\bar{2}$1	2.590	60	55	60	57
11$\bar{2}$2	2.561	100	99	100	99
10$\bar{1}$.10	2.493	8	8	2	4
11$\bar{2}$4	2.456	19	18	19	20
11$\bar{2}$5	2.385	32	31	32	31
10$\bar{1}$.11	2.329	–	–	2	1
20$\bar{2}$1	2.248	15	13	13	12
20$\bar{2}$2	2.225	8	13	16	15
20$\bar{2}$3	2.196	17	6	9	10
20$\bar{2}$4	2.155	7	11	10	10
11$\bar{2}$8	2.135	30	29	30	29
20$\bar{2}$5	2.108	3	5	11	6

10$\bar{1}$8 are of similar intensity in the case of 3*T-tv* structure, whereas in the 3*T-cv*1 variety the 10$\bar{1}$4 peak is notably stronger than the other three. Also, there are minor differences in intensity distribution of the 20$\bar{2}$*l* reflections in the two XRD patterns.

Importantly, the intensity distribution in the XRD pattern simulated for the 3*T-cv*2 structure differs substantially from those for both the 3*T-tv* and 3*T-cv*1 structures. First, the 10$\bar{1}$4 peak has nearly disappeared. Second, the 10$\bar{1}$2 (d = 4.313 Å) and 10$\bar{1}$3 (d = 4.104 Å) reflections for the 3*T-cv*2 structure are fairly strong while for both 3*T-tv* and 3*T-cv*1 they are quite weak. In addition, the 10$\bar{1}$8 reflection is considerably weakened in the XRD pattern for the 3*T-cv*2 structure.

In the XRD pattern simulated for the 3*T-cv*1/*cv*2 structure the intensity distribution in the region of 10$\bar{1}$*l* reflections appears to be intermediate between those for 3*T-cv*1 and 3*T-cv*2 structures (Table 7, figure not shown). Interestingly, in the patterns for the 3*T-cv*2 and 3*T-cv*1/*cv*2 structures the 10$\bar{1}$0 reflection (d = 4.500 Å) is stronger than the 10$\bar{1}$1 (d = 4.452 Å), whereas for the 3*T-tv* and 3*T-cv*1 structures, the 10$\bar{1}$1 peak intensity is greater than that for the 10$\bar{1}$0.

2O varieties

Figure 5 shows the XRD patterns simulated for the 2*O-tv* and 2*O-cv*1 structures. Reflection indices, positions and intensities for structures 2*O-tv*, 2*O-cv*1 and 2*O-cv*12 are given in Table 8. The peak positions are identical in the three XRD patterns. The main difference between the XRD patterns for the 2*O-tv* and 2*O-cv*1 varieties is that for the 2*O-tv* structure the 020, 110 peak at d = 4.502 Å is very strong and the 111 reflection (d = 4.391 Å), very weak; whereas for the 2*O-cv*1 structure these reflections are both quite strong, the latter being even stronger than the former. The 022, 112 (d = 4.105 Å) reflection for the 2*O-tv* structure is only slightly weaker than the 113 (d = 3.730 Å) peak; for
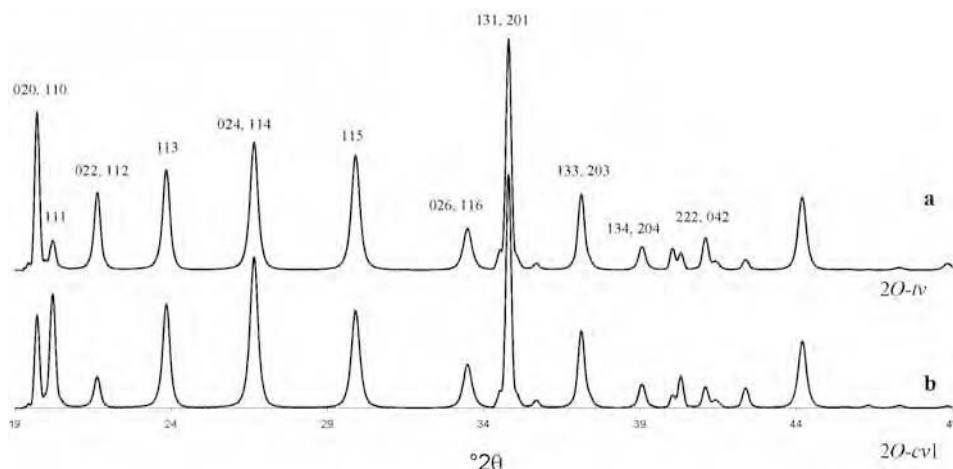
Figure 5. Simulated powder XRD patterns for structural models: (a) 2O-tv; and (b) 2O-cv1 (basal reflections are not shown). CuKα radiation.

the 2O-cv1 structure, the 022, 112 peak is much weaker than 113.

The XRD pattern for the 2O-cv12 structure (figure not shown) is practically identical to that for 2O-tv but for the relative intensities of the 022, 112 (d = 4.105 Å) and 113 (d = 3.730 Å) peaks: the 022, 112 peak intensity is slightly greater than that of 113 for the 2O-cv12 structure and *vice versa* for the 2O-tv structure.

DISCUSSION

Drits *et al.* (1984, 2006) showed that because of the specific structural distortions of *tv* and *cv* layers, the intralayer shift, layer offset and the overall interlayer stagger in 1M-cv illite structure differ from those in 1M-tv illite. In 1M-tv Al-rich illites the interlayer shift,

Table 8. Reflection indices, d_{hkl} values and relative peak intensities in the simulated XRD patterns for structural models 2O-tv, 2O-cv1 and 2O-cv12.

hkl	d_{hkl} (Å)	tv	cv1	cv12
			— I (%) —	
020, 110	4.502	69	40	61
111	4.391	12	49	12
022, 112	4.105	32	12	39
113	3.730	42	43	31
024, 114	3.343	54	63	70
115	2.987	49	41	40
026, 116	2.676	18	18	20
131, 201	2.578	100	100	100
132, 202	2.516	2	2	2
133, 203	2.421	30	31	32
134, 204	2.305	10	10	10
220, 040	2.251	9	6	5
221	2.237	7	12	12
222, 042	2.196	13	9	10
028, 118; 205, 135	2.180	3	2	3
223	2.132	4	8	8

i.e. the projection of the c axis on the *ab* plane ($c \times \cos \beta/a$) is equal to T_{tv} = −0.385 to −0.400, with $|T_{tv}|$ increasing with increasing octahedral Al content (Bailey, 1984; Brigatti and Guggenheim, 2002; Drits *et al.*, 1993; Zhukhlistov *et al.*, 1996). In 1M-cv Al-rich illites the values of $c \times \cos \beta/a$ (T_{cv}) vary from −0.300 to −0.315, with $|T_{cv}|$ increasing with decreasing octahedral Al content (Drits *et al.*, 1984, 1993). These differences in the unit-cell parameters lead to the differences in the positions of reflections having the same indices in the XRD patterns for 1M-tv and 1M-cv illite structures. The same reasons explain the differences in reflection positions for *tv* and *cv* 2M1 varieties, as well as those for *tv* and *cv* 2M2 structures. Therefore the *tv* 1M, 2M1 and 2M2 varieties of Al-rich micas can be distinguished from the corresponding *cv* varieties using powder XRD diffraction provided that the d values are measured with high precision and accurately compared with those calculated from the unit-cell parameters for the corresponding *hkl* indices. Such inferences, however, should be treated with caution, as the T_{tv} values tend to decrease with increasing contents of octahedral Mg and/or Fe. For example, in the series muscovite-phengite-leucophyllite, $|T_{tv}|$ values decrease from ∼0.4 for muscovite to 0.385 for phengite (Brigatti and Guggenheim, 2002 and references therein) and to 0.355 for leucophyllite (Sokolova *et al.*, 1976). In celadonites, these values range from 0.35 to 0.36 (Bailey, 1984; Muller *et al.*, 2000). Taking into account that for micas of the same composition having the same a, b and $c \times \sin \beta$, T_{cv} = $(1 + T_{tv})/2$ (Drits *et al.*, 1984, 2006), the differences in reflection positions for *tv* and *cv* varieties should decrease with increasing Mg and/or Fe contents, thus complicating their identification.

Additional complications should be expected in the case of structures containing stacking faults. All the XRD patterns (Figures 1−5) were simulated for defect-free structural models. The presence of stacking faults,

however, may strongly affect both peak positions and intensities, so that low-intensity peaks will disappear and subtle variations in intensity distribution will be modified (Drits and Tchoubar, 1990).

Problems in the identification of the trans-vacant and cis-vacant 1M and 3T varieties

Drits *et al.* (1993) noted that *trans*-vacant 3*T* and *cis*-vacant 1*M* mica polymorphs produce similar diffraction effects, *i.e.* in their powder XRD patterns *hkl* reflections have similar intensities and very close positions. Figures 1b and 4a,b show that the XRD pattern simulated for 1*M-cv* structure is similar to that for not only 3*T-tv*, but also 3*T-cv*1 variety. Indeed, the XRD patterns for the 3*T-tv* and 3*T-cv*1 structures are very much alike, as regards intensity distribution, especially if the $10\bar{1}6$ peak, which overlaps with the 009 reflection in an experimental XRD pattern, is ignored. The 1*M-cv* variety therefore can be easily confused with both 3*T* structures unless careful analysis of the peak positions is made. In accordance with the results of Drits *et al.* (1993) the positions of the reflections in the diagnostic region differ, so that $d_{111} > d_{10\bar{1}4}$, $d_{11\bar{2}} < d_{10\bar{1}5}$, $d_{112} > d_{10\bar{1}7}$ and $d_{11\bar{3}} < d_{10\bar{1}8}$ (Tables 4, 7), where 11*l* and $10\bar{1}l$ indices correspond to the 1*M-cv* and 3*T* varieties, respectively. Therefore if, after indexing and calculating the *d* values in terms of the 3*T* unit-cell, the following relationships are valid:

$$d_{calc}(10\bar{1}4) < d_{exp}(10\bar{1}4); \quad d_{calc}(10\bar{1}5) > d_{exp}(10\bar{1}5);$$
$$d_{calc}(10\bar{1}7) < d_{exp}(10\bar{1}7); \quad d_{calc}(10\bar{1}8) > d_{exp}(10\bar{1}8),$$

then the sample under study is probably not a 3*T* variety, and the XRD pattern should be re-indexed and *d* values should be re-calculated in terms of the 1*M-cv* unit-cell.

On the other hand, Figures 1a and 4c and Tables 4 and 7 show that both the peak positions and intensity distribution in the XRD pattern for the 3*T-cv*2 structure are very similar to those for the 1*M-tv* variety. Although 3*T-cv*2 structures have not been reported so far, theoretically the two varieties could be confused unless the differences in the actual positions of the reflections in the diagnostic region are taken into account, *i.e.* $d_{111} < d_{10\bar{1}4}$, $d_{11\bar{2}} > d_{10\bar{1}5}$, $d_{112} < d_{10\bar{1}7}$ and $d_{11\bar{3}} > d_{10\bar{1}8}$ (Tables 4, 7), where 11*l* and $10\bar{1}l$ indices correspond to the 1*M-tv* and 3*T* varieties, respectively. In addition, an important diagnostic feature of the 1*M-tv* structure, which distinguishes it from other mica varieties, is the presence of four reflections in the region of *d* between 2.50 and 2.35 Å (Figure 1a, Table 4): $20\bar{2}$ (*d* = 2.474 Å), 131 (*d* = 2.446 Å), $13\bar{2}$ (*d* = 2.396 Å) and 201 (*d* = 2.361 Å). In this region, the 3*T-cv*2 variety only shows two reflections, $11\bar{2}4$ at *d* = 2.456 Å and $11\bar{2}5$ at *d* = 2.385 Å (Figure 4c, Table 7).

Tables 4 and 7 show that the *d* values for the four diagnostic $10\bar{1}l$ reflections of the 3*T* varieties are intermediate between the *d* values for the respective 11*l* reflections of the 1*M-tv* and 1*M-cv* structures.

The similarities and dissimilarities in intensity distribution between the XRD patterns simulated for the 1*M* and 3*T* varieties in question may be associated with the differences in the mutual arrangement of cations and anions in successive layers in these structures. Drits and Sakharov (2004) noted that if a *cis*-vacant layer with the vacancy in the right-hand *cis* site (*cv*1 layer in our notation) is rotated counter-clockwise with respect to the preceding *cv*1 layer by 120º (as in the 3*T-cv*1 structure), then, in the normal projection on the *ab* plane, one of the two sets of symmetrically independent octahedral cations of the upper layer will almost superimpose on the OH groups in the lower oxygen plane of the octahedral sheet of the preceding layer. The other half of the octahedral cations will almost superimpose on the tetrahedral cations in the lower sheet of the preceding layer. On the other hand, for 120º counter-clockwise rotation of a *cv*2 layer with respect to the preceding one, which is realized in the 3*T-cv*2 structural model, all the octahedral cations will project almost onto the tetrahedral cations in the lower sheet of the preceding layer. In the 1*M-cv* structure, the arrangement of cations and anions in successive layers is similar to that in the 3*T-tv* and 3*T-cv*1 varieties. At the same time, in the 1*M-tv* structure, all octahedral cations project almost onto the tetrahedral cations in the lower sheet of the preceding layer in the same way, as in the 3*T-cv*2 structure. This may be the reason why the XRD pattern for the 1*M-cv* structure is similar to those for the two 3*T-tv* and 3*T-cv*1 varieties, whereas the XRD pattern for 1*M-tv* variety is similar to that for the 3*T-cv*2 structural model.

Another structural peculiarity of the mica varieties in question is the different disposition of anions across the interlayer. Because of the vacant octahedra being larger than those occupied by cations, the adjacent tetrahedra tilt over the vacant octahedral site, so that one of the three bridging basal oxygens moves inside the layer. The depressed oxygen atoms form grooves on the upper and lower basal tetrahedral surfaces (Bailey, 1984). In the 1*M-tv* structure, the grooves formed by the rows of depressed oxygens in the lower tetrahedral sheet of the upper layer will project onto those in the upper tetrahedral sheet of the preceding layer. As a result, in the distorted O octahedron around interlayer K, the two edges formed by the nearest depressed oxygens of the adjacent tetrahedral sheets will be significantly longer than the other four. In a *cv* 2:1 layer the upper and lower tetrahedral sheets are rotated by 120º with respect to each other. Therefore in the 1*M-cv* structure the grooves in the basal tetrahedral surfaces across the interlayer are rotated by 120º with respect to each other, as in the 3*T-tv* structure. Consequently, each depressed oxygen has a non-depressed oxygen for a nearest neighbor across the interlayer, so that the corresponding O−O distances are partly equalized (Drits *et al.*, 2006). Counter-clockwise rotation of a *cv*2 layer by 120º with respect to the preceding one, as in the 3*T-cv*2 structure, will lead to the

arrangement of anions across the interlayer that is similar to that in the $1M$-cv, $2M_1$-tv and $3T$-tv varieties. In contrast, if a $cv1$ layer is counter-clockwise rotated by 120º with respect to the preceding one, as in the $3T$-$cv1$ structure, the interlayer configuration will be the same as in the $1M$-tv structure.

The similarity between the XRD patterns for $3T$-tv, $3T$-$cv1$ and $1M$-cv, as well as that between the XRD patterns for the $1M$-tv and $3T$-$cv2$ structures show that from the point of view of diffraction, the differences in the interlayer structure are probably less significant than the disposition of octahedral cations with respect to the cations and anions of the preceding layer. However, both structural features might affect the relative stability of the mica varieties in question. Specifically, the pattern in the cation-cation and cation-anion superposition, as well as the arrangement of anions across the interlayer act favorably in the $1M$-cv and $3T$-tv structures. The $3T$-$cv1$ variety has favorable superposition of cations and anions in successive layers and $3T$-$cv2$, a better interlayer arrangement, whereas both factors are unfavorable in the $1M$-tv structure. The actual stability and abundance of the various mica polytypes and polymorphs, however, do not correlate directly with the above structural features and may be affected by other reasons. Taking into account the wide abundance of Al-rich $1M$-tv illite (Drits et al., 2006), $2M_1$-tv and $3T$-tv micas (Brigatti and Guggenheim, 2002; Pavese et al., 2001) we can conclude that one of the most significant factors governing the relative stability of tv and cv mica varieties may be the symmetric structure of the tv 2:1 layer and the asymmetry of the octahedral sheet of a cv layer (Drits et al., 2006). Further research will be needed to clarify the actual role of these factors.

Although numerous examples of $3T$-tv white micas have been reported (Brigatti and Guggenheim, 2002), there have been no reliable data on the occurrence of $3T$ illites. The possible existence of either tv or cv $3T$ illites remains therefore a matter of further investigation.

Identification of $2M_2$-tv and $2M_2$-cv varieties

Problems in the discrimination between the tv and cv $2M_2$ varieties may arise when the Mg and/or Fe content increases, so that the positions of the diagnostic reflections $20\bar{4}$, $11\bar{4}$, 114 and 204 in the tv and cv structures, respectively, become closer. In this case, special attention should be paid to the shape of the reflections, bearing in mind that the $2M_2$-tv structure shows sharp $20\bar{4}$ and 204 peaks, whereas the cv varieties show broadened peaks owing to partial overlap of $20\bar{4}$ and 113, and that of 204 and $11\bar{5}$ reflections. An additional diagnostic criterion is the triplet of $31\bar{4}$, 023 and 312 reflections in the XRD pattern for the $2M_2$-tv structure *vs.* a single 023 reflection for the cv $2M_2$ varieties.

Radoslovich (1960) was the first to note the similarities between XRD powder patterns of $2M_2$-tv

mica and a mixture of $1M$-tv and $2M_1$-tv micas. Analysis of Tables 4, 5 and 6 and Figures 1, 2 and 3 shows, however, that the $2M_2$ variety can be distinguished from mixtures of $1M$ and $2M_1$ polytypes using powder XRD. The main diagnostic feature of the simulated XRD pattern for $2M_2$-tv variety is the presence of a fairly intense reflection at 2.421 Å (023), which is absent in both $1M$-tv and $2M_1$-tv varieties. On the other hand, the XRD pattern for $2M_2$-tv structure does not contain reflections at ~3.730 Å (023 of $2M_1$-tv), 2.676 Å (023 of $1M$-tv), 2.561−2.567 Å (131 of $2M_1$-tv and $13\bar{1}$ of $1M$-tv, respectively) and some others. These results are in general agreement with the data of Shimoda (1970), who compared powder XRD patterns for two $2M_2$ illite samples with those for natural and artificial mixtures of $1M$ and $2M_1$ illites. However, accurate indexing based on the comparison of the simulated d values with those calculated from the corresponding unit-cell parameters allowed the present authors to provide more accurate indices for some of the reflections than those of Shimoda (1970).

Superstructure reflections in the $2M$-$cv12$ structure

The weak maxima present in the XRD pattern of the $2M$-$cv12$ structure at 4.396 Å (021), 3.965 Å ($11\bar{2}$), 3.729 Å (023), 3.489 Å (114), 3.201 Å ($11\bar{4}$), 2.987 Å (025) and 2.793 Å (116) (Figure 1c, Table 5) correspond to the positions of the 021, 112, 023, $11\bar{4}$, 114, 025 and $11\bar{6}$ reflections of the $2M_1$-tv structure, respectively (Figure 2a, Table 5). This can be explained as follows.

As the $2M$-$cv12$ structure consists of regularly alternating $cv1$ and $cv2$ layers packed as in the $1M$ polytype, the displacement between the successive layers is $-0.3085a$ and the resulting $c \times \cos \beta / a = -0.617$, or, for an alternative choice of the c axis, $+0.383$. This value is equal to $|c \times \cos \beta / a|$ of the $2M_1$-tv structural model, with c of the $2M$-$cv12$ structure equal to that of the $2M_1$-tv structure and $\beta = 180º - \beta$ ($2M_1$-tv) (Table 3). As a consequence, weak superstructure reflections with d values corresponding to the $2M_1$-tv structure appear between intense reflections that refer to the $1M$-cv structure (Table 5, Figure 1c). The indices of the superstructure reflections are related to those of the $2M_1$-tv structure so that $l(2M$-$cv12) = -l(2M_1$-$tv)$ for the $11l$ reflections and $l(2M$-$cv12) = l(2M_1$-$tv)$ for the $02l$ reflections. For the $11l$ and $02l$ reflections that coincide with those in the XRD pattern for the $1M$-cv structure, $l(2M$-$cv12) = 2l(1M$-$cv)+1$ and $l(2M$-$cv12) = 2l(1M$-$cv)$, respectively.

Possible interstratification of tv and cv layers

The identification of dioctahedral mica polytypes and polymorphs will become even more difficult if tv and cv layers are interstratified within the same structure. Such interstratification often occurs in illites and illite fundamental particles in I-S (Drits, 2003 and references therein).

As d values for the four diagnostic $10\bar{1}l$ reflections of the $3T$ varieties are intermediate between the d values for the respective $11l$ reflections of the $1M$-tv and $1M$-cv structures, it should be especially difficult to distinguish between the various $3T$ structures and interstratified tv/cv varieties with the layers packed as in the $1M$ structure. Indeed, according to the generalization of Méring's (1949) rules by Drits and McCarty (1996), the non-basal reflections of an interstratified structure are located between the neighboring hkl reflections of the periodic phases whose elementary layer units are interstratified. The positions of these reflections depend on the relative proportions of the interstratified interlayer translations. Therefore in a $1M$ structure in which tv and cv layers are interstratified, $11l$ reflections are located between the $11l$ reflections corresponding to pure tv and pure cv micas (Drits and McCarty, 1996; Drits, 2003). A case of special interest would be that where the ratio of randomly interstratified tv to cv layers is 1:2, so as to ensure $c \times \cos \beta/a = -1/3$. The positions of reflections will then be exactly identical to those expected for the $3T$ structure. As the cv layers prevail, the intensity distribution will be similar to that for the $3T$-tv and $3T$-$cv1$ structures. Therefore it will be extremely difficult or even impossible to distinguish between such a $1M$-tv/cv structure, on the one hand, and the $3T$-tv and $3T$-$cv1$ structures, on the other hand, using powder XRD. To do this, application of alternative diffraction methods is required. This problem is similar to that of the distinction between powder XRD patterns of trioctahedral $1M$ and $3T$ mica structures (Brigatti and Guggenheim, 2002),

Drits and Sakharov (2004) found that both the positions and shapes of hkl reflections in simulated XRD patterns of the $2M_1$-tv and $3T$-tv mica varieties are very similar to those for the interstratified $2M_1$-tv/cv and $3T$-tv/cv structures, respectively. Note that the similarity between the XRD patterns for the $3T$-tv and $3T$-tv/cv varieties is only observed when it is tv and $cv1$ layers that are interstratified in the $3T$-tv/cv structure. The qualitative XRD identification of these varieties is especially complicated when the number of cv layers is either small (10−15%) or large (30−40%) with significant tendency to segregation of the layer types. As shown by Drits and Sakharov (2004), partial occupancy of the *trans*-octahedral sites reported by Pavese *et al.* (2001) in phengite $3T$ cannot be explained in terms of random $\pm b/3$ slips but is probably associated with the interstratification of tv and cv layers within the phengite structure.

Further research is required to reveal reliable diffraction criteria for the identification of mica varieties with interstratified tv and cv layers.

CONCLUSIONS

Analysis of the simulated XRD patterns has provided a number of diffraction criteria that form a basis for the identification of dioctahedral mica structural varieties. At the same time, the apparent, as well as real, similarities revealed in the XRD patterns for various dioctahedral mica varieties lead to serious complications. High-precision measurements of the d values and their accurate comparison with the values calculated from the unit-cell parameters for the corresponding hkl indices are crucial for reliable identification. This, however, is a condition that is necessary but not always sufficient, and in some cases the only possible identification method would consist of simulation of diffraction effects for structural models and comparison of simulated and experimental XRD patterns. Further research should therefore be directed at the application of simulation and Rietveld refinement techniques, with account taken of possible interstratification of tv and cv layers and the presence of stacking faults. However, the interpretation of powder XRD patterns of dioctahedral mica structural varieties should be treated with caution, bearing in mind the inherent limitations in the method. For example, reliable and unambiguous identification of the $3T$-tv vs $3T$-$cv1$ structures, as well as the distinction between these two structures and the interstratified $1M$-tv/cv structure with the ratio of tv to cv layers of 1:2, may require application of alternative diffraction methods.

REFERENCES

Altaner, S.P. and Ylagan, R.F. (1997) Comparison of structural models of mixed-layer illite-smectite and reaction mechanisms of smectite illitization. *Clays and Clay Minerals,* **45,** 517−533.

Bailey, S.W. (1984) Crystal chemistry of the true micas. Pp. 13−66 in: *Micas* (S.W. Bailey, editor), Reviews in Mineralogy, **13,** Mineralogical Society of America, Washington, D.C.

Brigatti, M.F. and Guggenheim, S. (2002) Mica crystal chemistry and the influence of pressure, temperature and solid solution on atomistic models. Pp. 1−97 in: *Micas: Crystal Chemistry and Metamorphic Petrology* (A. Mottana, F.E. Sassi, J.B. Thompson Jr. and S. Guggenheim, editors). Reviews in Mineralogy and Geochemistry, **46,** Mineralogical Society of America, Washington, D.C. with Accademia Nazionale dei Lincei, Roma, Italy.

Cuadros, J. and Altaner, S.P. (1998a) Characterization of mixed-layer illite-smectite from bentonites using microscopic, chemical and X-ray methods: constraints on the smectite-to-illite transformation mechanism. *American Mineralogist*, **83,** 762−774.

Cuadros, J. and Altaner, S.P. (1998b) Compositional and structural features of the octahedral sheet in mixed-layer illite-smectite from bentonites. *European Journal of Mineralogy*, **10,** 111−124.

Drits, V.A. (2003) Structural and chemical heterogeneity of layer silicates and clay minerals. *Clay Minerals*, **38**, 403−432.

Drits, V.A. and McCarty, D.K. (1996) A simple technique for a semi-quantitative determination of the *trans*-vacant and *cis*-vacant 2:1 layer contents in illites and illite-smectites. *American Mineralogist*, **81**, 852−863.

Drits, V.A. and Sakharov, B.A. (2004) Potential problems in the interpretation of powder X-ray diffraction patterns from fine-dispersed $2M_1$ and $3T$ dioctahedral micas. *European Journal of Mineralogy*, **16**, 99−110.

Drits, V.A. and Tchoubar, C. (1990) *X-ray Diffraction of Disordered Lamellar Structures. Theory and Application to Microdivided Silicates and Carbons*. Springer Verlag, 242 pp.

Drits, V.A., Plançon, A., Sakharov, B.A., Besson, G., Tsipursky, S.I. and Tchoubar, C. (1984) Diffraction effects calculated for structural models of K-saturated montmorillonite containing different types of defects. *Clay Minerals*, **19**, 541−562.

Drits, V.A., Weber F., Salyn, A. and Tsipursky, S. (1993) X-ray identification of $1M$ illite varieties. *Clays and Clay Minerals*, **28**, 185−207.

Drits, V.A., Salyn, A.L. and Šucha, V. (1996) Structural transformations of interstratified illite-smectites from Dolna Ves hydrothermal deposits: dynamics and mechanisms. *Clays and Clay Minerals*, **44**, 181−190.

Drits, V.A., Środoń, J. and Eberl, D.D. (1997) XRD measurement of mean illite crystallite thickness: Reappraisal of the Kübler index and the Scherrer equation. *Clays and Clay Minerals*, **45**, 461−475.

Drits, V.A., Lindgreen, H., Salyn, A.L., Ylagan, R. and McCarty, D.K. (1998) Semiquantitative determination of *trans*-vacant and *cis*-vacant 2:1 layers in illites and illite-smectites by thermal analysis and X-ray diffraction. *American Mineralogist*, **83**, 31−73.

Drits, V.A., Lindgreen, H., Sakharov, B.A., Jakobsen, H.J., Salyn, A.L. and Dainyak, L.G. (2002) Tobelitization of smectite during oil generation in oil-source shales. Application to North Sea illite-tobelite-smectite-vermiculite. *Clays and Clay Minerals*, **50**, 82−98.

Drits, V.A., McCarty, D.K. and Zviagina, B.B. (2006) Crystal-chemical factors responsible for the distribution of octahedral cations over *trans*- and *cis* sites in dioctahedral layer silicates. *Clays and Clay Minerals*, **54**, 131−152.

Ey, F. (1984) Un exemple de gisement d'uranium sous discordance: les minéralisations Protérozoiques de Cluff Lake, Saskatchewan, Canada: Thèse de doctorat, Université Louis Pasteur, Strasbourg 1, France.

Halter, G. (1988) Zonalité des altérations dans l'environnement des gisements d'uranium associés à la discordance du Protérozoïque moyen (Saskatchewan, Canada). Thèse de doctorat, Université Louis Pasteur, Strasbourg 1, France.

Lanson, B., Beaufort, D., Berger, G., Baradat, J. and Lacharpaque, J.C. (1996) Illitization of diagenetic kaolinite-to-dickite conversion series: Late-stage diagenesis of the Lower Permian Rotliegend sandstone reservoir, offshore of the Netherlands. *Journal of Sedimentary Research*, **66**, 501−518.

Lee, M. (1996) $1M$(cis) illite as an indicator of hydrothermal activities and its geological implication. *33rd Annual meeting of the Clay Minerals Society, program and abstracts*. Gatlinburg, Tennessee, 1996, p.106.

Lindgreen, H., Drits, V.A., Sakharov, B.A., Salyn, A.L., Wrang, P. and Dainyak, L.G. (2000) Illite-smectite structural changes during metamorphism in black Cambrian Alum shales from the Baltic area. *American Mineralogist*, **85**, 1223−1238.

McCarty, D.K. and Reynolds, R.C. Jr. (1995) Rotationally

disordered illite-smectite in Paleozoic K-bentonites. *Clays and Clay Minerals*, **43**, 271−284.

McCarty, D.K. and Reynolds, R.C. Jr. (2001) Three-dimensional crystal structures of illite-smectite minerals in Paleozoic K-bentonites from the Appalachian basin. *Clays and Clay Minerals*, **49**, 24−35.

Méring, J. (1949) L'interférence des rayons X dans las systèmes à stratification désordonnée. *Acta Crystallographica*, **2**, 371−377.

Méring, J. and Oberlin, A. (1971) Smectites. Pp. 193−229 in: *The Electron-Optical Investigation of Clays* (J.A. Gard, editor). Monograph **2**, Mineralogical Society, London.

Muller, F., Drits, V.A., Plançon, A. and Besson, G. (2000) Dehydroxylation of Fe^{3+}, Mg-rich dioctahedral micas: (I) structural transformation. *Clay Minerals*, **35**, 491−504.

Pavese, A., Ferraris, G., Pishedda, V. and Fauth, F. (2001) M1-site occupancy in $3T$ and $2M_1$ phengites by low temperature neutron powder diffraction: reality or artefact? *European Journal of Mineralogy*, **13**, 1071−1078.

Plançon, A. (1981) Diffraction by layer structures containing different kinds of layers and stacking faults. *Journal of Applied Crystallography*, **14**, 300−304.

Plançon A. and Tchoubar, C. (1977) Determination of structural defects in phyllosilicates by X-ray powder diffraction. I. Principle of calculation of the diffraction phenomenon. *Clays and Clay Minerals*, **25**, 430−435.

Plançon, A., Tsipursky, S.I. and Drits, V.A. (1985) Calculation of intensity distribution in case of oblique texture electron diffraction. *Journal of Applied Crystallography*, **18**, 191−196.

Radoslovich, E.W. (1960) Hydromuscovite with the $2M_2$ structure − A criticism. *American Mineralogist,* **45**, 894−898.

Reynolds, R.C., Jr. (1993) Three-dimensional X-ray diffraction from disordered illite: simulation and interpretation of the diffraction patterns. Pp. 44−78 in: *Computer Applications to X-ray Diffraction Methods* (R.C. Reynolds and J. Walker, editors). Workshop Lectures **5,** The Clay Minerals Society, Bloomington, Indiana.

Reynolds, R.C. Jr. and Thomson, C.H. (1993) Illites from the Postam sandstone of New York, a probable noncentrosymmetric mica structure. *Clays and Clay Minerals*, **41**, 66−72.

Sakharov, B.A., Naumov, A.S. and Drits, V.A. (1982) X-ray diffraction by mixed-layer structures with random distribution of stacking faults. *Doklady Akademii Nauk SSSR,* **265**, 339−343 (in Russian).

Shimoda, S. (1970) A hydromuscovite from the Shakanai mine, Akita Prefecture, Japan. *Clays and Clay Minerals*, **18**, 269−274.

Smoliar-Zviagina, B.B. (1993) Relationships between structural parameters and chemical composition of micas. *Clay Minerals*, **28**, 603−624.

Sokolova, T.N., Drits, V.A., Sokolova, A.L. and Stepanov, S.S. (1976) Structural and mineralogical characteristics and conditions of formation of leucophyllite from salt-bearing deposits of Inder. *Litologiya and poleznye iskopaemye*, **6**, 80−95 (in Russian).

Warshaw, C.M (1959) Experimental studies of illites. *Clays and Clay Minerals*, **7**, 303−316.

Ylagan, R.F., Altaner, S.P. and Pozzuoli, A. (2000) Reaction mechanisms of smectite illitization associated with hydrothermal alteration from Ponza island, Italy. *Clays and Clay Minerals*, **48**, 610−631.

Zhukhlistov, A.P., Draguleska E.M., Rusinov, V.L., Kovalenker, V.A., Zvyagin, B.B. and Kuz'mina, O.V. (1996) Sericite with non centorosymmetric structure from gold-silver-polymetallic ores of Banska Stiavnica deposit (Slovakia). *Zapiski Vserossiyskogo Mineralogicheskogo Obshchestva*, **125,** 47−54 (in Russian).

Zvyagin B.B. (2001) Current problems with the nomenclature of phyllosilicates. *Clays and Clay Minerals*, **49**, 492−499.

Zvyagin, B.B., Rabotnov, V.T., Sidorenko, O.V. and Kotelnikov D.D. (1985) Unique mica consisting of non-centrosymmetric layers. *Izvestiya Akademii Nauk S.S.S.R, Seriya Geologicheskaya*, **35**, 121−124 (in Russian).